Jin Shang , Huai-Yu Zhong , Hong-Liang Zhang , Bin Li , Xiao-Xue Wang , Fu-Yun Zhao , Yuguo Li. (2023).
Diode effects on street canyon ventilation in valley city: Temperature inversion and calm geostrophic wind.*Building and Environment*.
doi: 10.1016/j.buildenv.2023.110839

Diode effects on street canyon ventilation in valley city: Temperature inversion and calm geostrophic wind

Jin Shang

Huai-Yu Zhong

Hong-Liang Zhang

Bin Li

Xiao-Xue Wang

Fu-Yun Zhao

Yuguo Li

School of Power and Mechanical Engineering, Wuhan University, Wuhan, Hubei Province, PR China
School of Energy and Environment, Anhui University of Technology, Ma-An-Shan, Anhui Province, 243002, PR China
Department of Mechanical Engineering, University of Hong Kong, Pokfulam Road, Hong Kong, PR China
School of Information and Communication, Shenzhen Institute of Information Technology, Shenzhen, PR China

Corresponding author: Fu-Yun Zhao, School of Power and Mechanical Engineering, Wuhan University, Wuhan, Hubei Province, PR China
Email address: zfycfdnet@163.com

Submitted to *Building and Environment* July 13 2023

Accepted September 2023

Author Biographies

Jin Shang, was researched in School of Power and Mechanical Engineering, Wuhan University, Wuhan, Hubei Province, PR China.

Huai-Yu Zhong, PhD, is Lecturer in the School of Energy and Environment, Anhui University of Technology, Ma-An-Shan, Anhui Province, 243002, PR China. His research interests are in indoor airflow dynamics and contaminant dispersion. His current research topics include human-induced particle resuspension, stratified ventilation performance in large enclosures, and interaction between thermal plumes and room air distribution.

Hong-Liang Zhang, was researched in School of Power and Mechanical Engineering, Wuhan University, Wuhan, Hubei Province, PR China.

Bin Li, was researched in School of Power and Mechanical Engineering, Wuhan University, Wuhan, Hubei Province, PR China.

Xiao-Xue Wang obtained his PhD at the University of Hong Kong. His research interests are in indoor air quality control.

Fu-Yun Zhao, PhD, is Professor in the School of Power and Mechanical Engineering, Wuhan University, Wuhan, Hubei Province, PR China. His research interests are in heat and mass transfer in built environments and renewable energy utilization. His current research topics include double-diffusive convection in ventilated spaces, solar-assisted natural ventilation, and coupled indoor-outdoor pollutant transport modeling.

Yuguo Li, PhD, is Chair Professor of Building Environment, Honorary Professor of School of Public Health, Associate Dean (Research) of Engineering. His research interests are in building environment engineering. His current research topics include city climate/environment, environment studies of infection and indoor environment.

Diode effects on street canyon ventilation in valley city: Temperature inversion and calm geostrophic wind

Abstract

In urban areas, especially in valleys, challenges from heat and pollution are common. The situation worsens due to temperature inversions, where warm air traps pollutants. A new study employed multi-scale computational fluid dynamics (CFD) to assess ventilation in valley cities, specifically during temperature inversions and calm winds. Parameters like air change rate (ACH), local mean age of air (LMAA), and purging flow rate (PFR) were used to gauge street canyon ventilation efficiency. Factors such as atmospheric stability, city-slope positioning, and surface materials are altered to analyze impacts on urban heat island (UHI) intensity and air quality.

Results indicated that katabatic winds had varied effects on pollution in different city regions, influenced by atmospheric conditions. Higher temperature lapse rates led to enhanced pollutant removal near slopes due to vortex interactions, but distant regions experienced thicker inversion layers, limiting pollutant dispersion. Conversely, anabatic winds improved ventilation with distance. Under inversion conditions, slope-city distance and surface materials played roles.

For katabatic winds, city positioning significantly reduced UHI intensity, lowering LMAA by around 440s. Anabatic winds' UHI impacts ranked as atmospheric conditions, city location, and surface materials. A neutral atmosphere reduced UHI by 4.5K, but increased distance between city and slopes strengthened UHI by 4.04K. Ventilation efficiency was mainly tied to atmospheric conditions, while city location impacted pollution mitigation.

This research aids in understanding air quality and airflow patterns during extreme weather events, aiding urban canyon design in valleys, especially with recurring heatwaves.

(239 words)

Graphical abstract

In urban areas located within valley region, thermal and pollutant islands could become worsen due to temperature inversions, and even warm air traps pollutants. A multi-scale computational fluid dynamics (CFD) code was adopted to evaluate the ventilation in valley cities, specifically during temperature inversions and calm winds. Parameters like air change rate (ACH), local mean age of air (LMAA), and purging flow rate (PFR) were used to gauge street canyon ventilation efficiency. Factors such

as atmospheric stability, city-slope positioning, and surface materials are altered to analyze impacts on urban heat island (UHI) intensity and air quality.

< **Graphical abstract**>

Keywords

Valley city, Ventilation diode effect, Thermal stability condition, Temperature inversion, Self-proposed multiscale CFD

1.Introduction

1.1. "Urban heat island" "slope winds" and air quality

Urbanization has led to a concentration of population in cities and a subsequent increase in environmental issues, such as alterations to surface net energy balance and changes in atmospheric pollutant concentrations [1,2]. The high level of building and road density in urban regions leads to distinctive radiative, convective, conductive, and storage characteristics in contrast to surrounding terrain [3,4]. Moreover, the release rates of pollutants and heat are considerably higher due to the large traffic and energy demands in urban areas [5]. In cities of a certain scale, wind is key to mitigating these issues [6]. In general, strong winds can effectively remove excess heat from the city, whereas during calm weather conditions, the heat and pollutants tend to be trapped under the city dome, negatively impacting urban ventilation and human comfort [7,8]. Local winds can arise due to temperature variations between urban and rural areas and the existence of an inversion layer in the atmospheric temperature profile [9]. These winds are commonly known as the urban heat island circulation (UHIC) [10,11]. The characteristics of this circulation, including its direction and magnitude, are constrained by various factors, including atmospheric environmental parameters, urban surface characteristics, urban scale, and surrounding topography [12].

Cities situated in valleys experience exacerbated local environmental challenges [13]. As a result of the non-uniform thermal characteristics of the underlying surface, the "cold pool effect" can occur more readily in valleys, which strongly suppresses air convection [14,15]. Furthermore, the terrain's barrier effect exacerbates the deceleration of wind speed within urban areas, ultimately resulting in unfavorable conditions for atmospheric diffusion. In situations where a stagnant weather system coincides with a comparatively stable atmospheric structure, the likelihood of smoggy conditions increases [16].

In such situations, the ventilation of valley cities relies only on slope winds formed by natural thermal pressure and UHIC due to the lack of large-scale background winds. Therefore, investigating the effects of the interaction of slope winds and urban heat islands on pollutant emissions is of great importance.

In current research, the factors affecting the intensity of the urban heat island include urban scale [17], urban morphology [18], building height [19], and anthropogenic heat [20]. For valley cities, the factors include angle of slope wind [21], the height of buildings [22]and anthropogenic heat flux [23]. Few studies have focused on the

effect of vertical background temperature variation and existence of inversion [22,24]. Furthermore, urban areas are commonly regarded as planar surfaces characterized by a uniform heat flux or a simplistic urban parameterization in these studies, with no consideration of the microscale structure of the urban canopy [24], which is fairly important in densely built-up areas.
Moreover, the flow characteristics and magnitude of mesoscale circulation phenomena, such as UHIC and slope winds, are intricately linked to atmospheric vertical stability and wind speed. Specifically, the vertical thermal gradient governs the maximum altitude of UHIC as well as the horizontal extent of the flow pattern [12]. In the limited CFD studies, the influence of atmospheric stratification and the existence of inversion on this phenomenon is often ignored, leading to inaccuracies in predicting the vertical flows.

Meanwhile, the presence of temperature inversions is highly detrimental to the dispersion of pollutants and exacerbates the formation of urban heat islands and pollution islands within cities. Under inversion conditions, a stable layer of warm air is trapped above the cooler air near the surface, preventing the vertical mixing of pollutants and leading to their accumulation. This trapped layer of warm air also intensifies the urban heat island effect, as the heat generated by human activities and urban structures becomes trapped within the city, further raising temperatures. Therefore, it is crucial to conduct parameterized studies specifically focusing on the characteristics and impacts of temperature inversions in valley cities. By understanding the factors contributing to inversion formation and their effects on pollutant dispersion and urban climate, effective mitigation strategies can be developed to alleviate the adverse effects of temperature inversions and improve air quality and thermal conditions in valley cities.

1.2. Various methods for studying mesoscale airflow

Various methods including field measurements, theoretical analyses, model experiments, and numerical simulations have been employed to study mesoscale air flows [25]. Particularly, experiments with water tanks and numerical simulations have demonstrated notable advantages and encouraging potential for investigating mesoscale flows, warranting further consideration from researchers [26]. Numerical simulations in this field can be broadly classified into two categories [27]. One is numerical models that are adept at mesoscale simulations, such as weather forecast models like the Weather Research and Forecasting model (WRF), which ignores details within the urban canopy layer [28]. The other is Computational Fluid Dynamics (CFD) methods that are skilled in small-scale simulations [29]. Their greatest advantage lies in reducing research costs and shortening research cycles [30]. However, traditional CFD methods have not considered atmospheric stratification effects, making their extension to the urban scale of great importance. Especially in cross-scale situations, such as urban heat island (UHI) and slope winds, where near-field and far-field flow characteristics are both critical [31].

Kristof et al. present a mathematical demonstration that by introducing additional source terms, and the Coriolis force can be included in the governing equations of micro-scale computational fluid dynamics (CFD) to render them equivalent to those of mesoscale flows, as demonstrated by previous research [32]. By utilizing this methodology, Wang and colleagues were able to effectively replicate the circulation

of urban heat island. They compared their results with those obtained through meteorological prediction models and water tank experiments, showing that their results were in good agreement with previous studies [33]. Mei et al. [34] employed computational fluid dynamics (CFD) techniques to examine the dispersion of air pollutants within a group of deep street canyons, in the presence of induced natural convection flow. The study found that the concentration of pollutants was greater in the canyons situated in the center of the city. Subsequently, Abbassi et al. [6] extended the methodology and evaluated the dispersion of pollutants within the urban heat island circulation across different atmospheric stability states.

In terms of experiments, Shindler and Moroni investigated the coupling effects between slope winds and UHIC through water tank experiments [35]. Shindler et al. examined the effects of the interplay between UHIC and slope winds in narrow mountain valleys under static weather conditions, using a laboratory model based on a temperature-stratified water tank. Afterward, Wu et al. introduced a numerical simulation methodology, referred to as the "numerical water tank," to examine mesoscale flows using a micro-scale approach. The authors also examined the unique effects of urban scale and changes in geometric shape on the characteristics of the mesoscale flow field in valley cities [24].

The literature review indicates that investigating the coupling of slope winds and urban heat island circulation is crucial for urban ventilation, yet the mechanisms and flow structures of their interaction remain unclear. Understanding the characteristics of local wind interactions can help to explore the transport mechanisms of regional pollutants, as the airflow pattern of slope winds varies significantly during different times of day.

In this study, we conducted numerical investigations to examine the interaction between idealized slope flows and urban heat island circulation, as well as the resulting distribution of pollutants and the intensity of the urban heat island within the urban canopy layer. A modified and validated computational fluid dynamics (CFD) method was employed in this research. At the same time, this study is the first to apply an temperature inversion model to investigate valley cities. The results of this study can provide theoretical reference for wind power layout in valley cities and urban canyon design, in order to improve the air quality and wind environment of urban street.

This article is organized as follows: The numerical simulation approach used in this study is described in detail in Section 2, including the configuration of the model. In Section 3, a comparison between the numerical simulation results and experimental data was conducted to assess the accuracy and reliability of the computational method employed in this study. In Section 4, we simulated the impacts of various factors, including atmospheric conditions, the relative positioning of the city and slope and the characteristics of urban/slope surface materials under inversion conditions, on the urban environment under both katabatic winds and anabatic winds conditions. The contributions of these factors to the urban heat island and air quality in valley cities were quantitatively compared. The relationships between katabatic and anabatic winds and urban air quality and the urban heat island were analyzed. The limitations of this study, as well as future research directions, and conclusions are discussed in detail in Sections 5 Limitations and future work, 6 Conclusions.

2. Physical modeling and numerical methods

2.1. Multi-scale model establishment

In this research, a pressure-based equation was formulated, which builds upon the model utilized by Kristof et al. [32] and the equations proposed by Wang and Li [33]. Ordinary CFD simulations cannot consider the properties of mesoscale circulation, so in order to better study the urban heat island problem across scales, this study improves the pressure-based solver to overcome the effects of atmospheric compressibility, hysteretic elasticity, and temperature layers such as inversion temperature.
The modification starts with the definition of different static atmospheric layers. It is assumed that the temperature distribution in the static atmospheric boundary layer is determined by the temperature distribution with constant decreasing rate ($\gamma = -\partial T/\partial y$) of the layers. Variables indicated by an apostrophe representing deviations from the static state (e.g. T', P', and ρ'). The real temperature, pressure, and density are represented as T, P, and ρ respectively. The compressible and unsteady Navier-Stokes equations are then incorporated into general-purpose computational fluid dynamics solvers. Kristof et al. [33] neglected that the transformation coefficient x also varies with the different reference state temperature lapse rates.

(1) Continuity equation

The derivation here mainly considers the compressibility of the atmosphere, the hysteresis approximation, and how it is implemented in the incompressible solver of CFD.

After considering the deviation from the static state we can get:

$$\frac{\partial(\rho_s + \rho')}{\partial t} + \nabla \cdot \left((\rho_S + \rho')\mathbf{U}\right) = 0 \tag{1}$$

By assuming $\rho' \ll \rho_s$, the continuity equation in an incompressible flow can be expressed as follows:

$$\nabla \cdot (\rho_0 U) = -\rho_0 \left| \frac{\nabla \rho_s}{\rho_s} \right| w \tag{2}$$

Because of $\gamma(z-z_0) \ll T_0$, ξ is considered constant.

$$\zeta = -\frac{(g / R_0) - \gamma}{T_v} \tag{3}$$

Finally, the continuity equation in its incompressible form is given as:

$$\nabla \cdot (\rho_0 U) = S_m \tag{4}$$

$$S_m = -\rho_0 w \zeta \tag{5}$$

Kristof et al. [32], Wang et al. [33] and Abbassi et al. [7] omitted this term from the continuity equation. The analysis suggests that the mass source term in the heat island circulation is of the order of O (−2), which is significantly smaller than the other terms in the equation and can be regarded as insignificant.

(2) Momentum equation

The derivation here is mainly to consider how the density stratification of the atmosphere on the vertical force is converted in the incompressible solver of CFD.

The inertial force density is replaced and the pressure is decomposed as follows:

$$(\rho_S + \rho')\frac{dU}{dt} = -\nabla(P_S + P') + \nabla\tau + \rho g \tag{6}$$

Considering $\rho' \ll \rho_s$, using the chain rule, the buoyancy term is substituted with a temperature-related function:

$$\frac{\partial \rho_0 U}{\partial t} + \nabla(\rho_0 U \times U) = -\frac{\rho_0}{\rho_s}\nabla P' + \nabla\left(\frac{\rho_0}{\rho_s}\tau\right) + \rho_0\beta(T)(\vartheta - T_0)\,|\,g\,|\,j - \tau\nabla\left(\frac{\rho_0}{\rho_s}\right) + US_m \tag{7}$$

The buoyancy term is substituted by the ground-based buoyancy term. Thus:

$$\beta(T) = \frac{1}{T_s} = \frac{1}{T_0}\frac{T_0}{T_s} = \beta_0\left(1 + \left(\frac{T_0}{T_s} - 1\right)\right) \tag{8}$$

$$\eta(z) = \left(\frac{T_0}{T_s} - 1\right) \tag{9}$$

Dynamic pressure perturbations are calculated in terms of the velocity magnitudes described by Bernoulli's equation, according to definition of buoyancy pressure perturbation term:

$$P_{b'} \approx \frac{\rho'}{\rho_s}\frac{\partial}{\partial z}g \tag{10}$$

$$\pi_{b'} \approx \frac{\rho'}{\rho_0}\frac{\partial}{\partial z}g \tag{11}$$

According to $(\rho_s/\rho_0)\partial(\rho_0/\rho_s)/\partial z = -\xi$ 和 $\xi \ll 1$,:

$$P_{b'} \approx \frac{1}{\rho_s}\frac{\partial}{\partial z}\rho' g \tag{12}$$

$$\pi_{b'} \approx \frac{1}{\rho_0}\frac{\partial}{\partial z}\rho' g \tag{13}$$

At high altitudes, inertial and viscous forces are negligible compared to object forces. Therefore, the dynamic pressure term should be balanced by the volumetric force as shown below:

$$\nabla \pi_{b'} = S_b \tag{14}$$

After the equation transformation, the momentum equation is

$$\frac{\partial \rho_0 U}{\partial t} + \nabla(\rho_0 U \times U) = -\pi' + \nabla \tau + \left(\frac{\rho_0}{\rho_s}\right)^2 S_b \tag{15}$$

$$S_b = \rho_0 \beta_0 (1 + \eta(z))(\vartheta - T_0) \mid g \mid j + U S_m \tag{16}$$

(3) Energy equation

Considering $dh=C_p(T)dT$, the derivation leads to the following equation:

$$\rho C_p \left[\frac{\partial T_s}{\partial t} + \mathbf{U} \cdot \nabla T_s\right] + \rho C_p \left[\frac{dT'}{dt}\right] - \left[\frac{\partial P_s}{\partial t} + \mathbf{U} \cdot \nabla P_s\right] - \left[\frac{dP'}{dt}\right] = \nabla \cdot k \nabla T + (\tau \nabla \cdot \mathbf{U}) + S_e \tag{17}$$

The energy equation can be reformulated by adding a constant reference temperature to the perturbation temperature derivative and using the resulting temperature as the incompressible temperature:

$$\frac{\partial(\rho_0 C_p \vartheta)}{\partial t} + \nabla\left(\rho_0 C_p \vartheta \mathbf{U}\right) = \nabla \cdot K_{\text{eff}} \nabla \vartheta + (\overline{\overline{\tau}} \nabla \cdot \mathbf{U}) + S_e \tag{18}$$

$$S_e = \left(\rho_0 C_p v \gamma - v \rho_0 \mid g \mid\right) + (T - T_0) S_m \tag{19}$$

$$K_{\text{eff}} = \frac{\rho_0}{\rho_s}\left(k + \frac{C_p \mu_t}{Pr_t}\right) = K + \frac{C_p}{Pr_t}\left(\rho_0 C_\mu \frac{k^2}{\varepsilon}\right) \tag{20}$$

(4)Turbulence kinetic energy and dispersion item

The assumptions made are consistent with those of the previous sections; therefore, the resulting form of the turbulent kinetic energy equation is as follows:

$$\frac{\partial(\rho_0 k)}{\partial t} + \nabla\left(\rho_0 k \mathbf{U}\right) = \nabla \cdot \left(\left(M + \frac{M_t}{\sigma_k}\right)\nabla k\right) + G_{k,0} + G_{b,0} - \rho\varepsilon + S_k \tag{21}$$

$$S_k = -\beta_0 \eta \mid g \mid \frac{M_t}{Pr_t}\frac{\partial T'}{\partial z} + \beta_0 (1 + \eta) g \frac{M_t}{Pr_t}\left(\gamma - \frac{g}{C_p}\right) + k + S_m \tag{22}$$

It should be noted that Abbassi et al. [7] did not replace T with the potential temperature θ when deriving the turbulence equations under static conditions, and their derivation of the turbulence equations and source terms showed some deviations. The treatment of the turbulence equations by Wang [33] and Kristof [32] is reasonable.

Repeating a similar derivation of the turbulent energy equation yields, pollutant diffusion equation can be derived as:

$$\rho \frac{d\varepsilon}{dt} = \nabla \cdot \left(\left(\mu + \frac{\mu_t}{\sigma_k} \right) \nabla \varepsilon \right) + C_{1\varepsilon} \frac{\varepsilon}{k} (G_k + C_{3\varepsilon} G_b) - C_{2\varepsilon} \rho \frac{\varepsilon^2}{k} + S_\varepsilon \quad (23)$$

$$\frac{\partial(\rho_0 \varepsilon)}{\partial t} + \nabla \left(\rho_0 \varepsilon \mathbf{U} \right) = \nabla \cdot \left(\left(M + \frac{M_t}{\sigma_k} \right) \nabla \varepsilon \right) + C_{1\varepsilon} \frac{\varepsilon}{k} (G_{k,0} + C_{3\varepsilon} G_{b,0}) - C_{2\varepsilon} \rho_0 \frac{\varepsilon^2}{k} + S_\varepsilon \quad (24)$$

$$S_\varepsilon = C_{1\varepsilon} \frac{\varepsilon}{k} C_{3\varepsilon} \left(\beta_0 (1+\eta) g \frac{M_t}{Pr_t} \left(\gamma - \frac{g}{C_p} \right) - \beta_0 \eta g \frac{M_t}{Pr_t} \frac{\partial T'}{\partial z} \right) + \varepsilon S_m \quad (25)$$

Furthermore, π represents the incompressible pressure. T_{ij} is the incompressible shear stress, T is the incompressible temperature, K is the incompressible thermal conductivity, M represents the incompressible viscosity and M_t represents the turbulence viscosity.

(5) Pollutant dispersion model

In this study, the gaseous pollutants of carbon monoxide (CO) is used to represent near-ground emissions of traffic exhaust. The transport equation of CO is shown as:

$$\overline{u_j} \frac{\partial C}{\partial x_j} - \frac{\partial}{\partial x_i} \left[\left(D_a + \frac{v_t}{Sc_t} \right) \frac{\partial C}{\partial x_j} \right] = S \quad (26)$$

where $\overline{u_j}$ is the average velocity vector in direction j, C is the time averaged concentration CO of the pollutant, g/m^3, D_a is the molecular diffusion coefficient, v_t is the turbulent diffusivity and S_{Ct} is the turbulent Schmidt number with the values of 0.7. S is a pollutant CO source term with a rate of emission of 1.25×10^{-6} kg/m^3/s. To ensure that the equations are correct, the equations are verified in Section 3.2.2.

2.2. Numerical simulation setup

In this study, the unsteady-state flow field is solved using Ansys FLUENT equipped with the *k-ε* model. This study used the standard k-ε model and standard wall function to introduce atmospheric stratification by UDF (user-defined-function) modifying the source and diffusion terms of the control equation. The temperature lapse rate is introduced through the use of a source term. The convective terms in the numerical computations were discretized utilizing a second-order upwind differencing scheme. The PISO (Pressure-Implicit with Splitting of Operators) algorithm was employed for the coupling of pressure and velocity [36]. The convergence condition was set to be that the residuals of all equations were below 10^{-4}.

After employing 10,000-time steps with transient simulation, once the data converged to stability, data collection was initiated. Through the simulation, it was observed that different sampling durations, namely 50,000s, 60,000s, and 70,000s, yielded nearly

indistinguishable outcomes. As a result, a sampling duration of 60,000s was ultimately chosen.

2.3. Models and computational domain

Fig. 1a illustrates a two-dimensional model that was constructed to examine the ventilation features of a hillside urban area in the presence of UHI. The decision to utilize 2D simulations stems from a trade-off between computational feasibility and capturing essential features of heat island flows over hillslopes. The 2D approach proves well-suited for investigating overarching trends, parameter sensitivity, and primary dynamics [37], aligning with the research's focus on assessing ventilation efficiency and heat island intensity.

<Fig.1>

The model comprises 20 blocks, with the city situated at the bottom of the model. *B* represents the length and height of the buildings in the urban area, and *h* represents the length of the city blocks. The entire calculation domain has a length of 8000 m and a height of 3000 m. In order to ensure the accuracy of the numerical simulation results, a grid refinement technique was implemented near the solid boundaries and interfaces. The horizontal grid spacing of the urban region is defined as 0.1 m along the x-axis. The grid spacing in the y-direction is gradually increased with a rate of 1.05, with the smallest grid spacing being 0.1 m. According to the requirements of the wall function method, the distribution of Y+ at the wall edge is between 30 and 160.

The two opposite sides of the computational domain are assumed to have the pressure outlet boundary condition applied, and the top boundary is assumed to be a symmetric boundary condition, and the time step is set as 1s. An absorption layer [38] is added below the top boundary of the calculation domain to avoid the influence of reflected waves. The heat fluxes of the city and hillside vary from case to case. For heat island simulation studies, urban heat fluxes of 30–200 W/m^2 at the bottom are generally considered [22,37,39], with a maximum of 300 W/m^2 [39]. A comprehensive investigation is carried out to examine the elements that affect urban ventilation for each category of slope wind, subsequently delving into their influence on the magnitude of urban heat islands. All cases are shown in Table 1.

<Table.1>

3. Accuracy of multi-scale model simulation

3.1. Grid sensitivity analysis

In order to ensure that the results of the CFD simulations are independent of the grid resolution, a grid sensitivity analysis is conducted. There are three kinds of grid, coarse (321,834 cells, the smallest cell size = 0.15 m), medium (852274 cells, the smallest cell size = 0.10 m), fine (1174645 cells, the smallest cell size = 0.10 m). Numerical uncertainty assessment in this study was accomplished using Roache's [40] proposed Grid Convergence Index (GCI) technique. This method, rooted in

Richardson extrapolation theory, entails contrasting discrete solutions on two grids with distinct spacings (h).

The grid convergence index (GCI) is used to establish grid independence, which is expressed by the following equation (Eq. (23)), as proposed by Roach.

$$GCI = F_s \left| \frac{r_p \left(u_{i,\text{grid\_A}} - u_{i,\text{grid\_B}}\right) / \left| U_{ref} \right|}{1 - r_p} \right| \tag{27}$$

In Eq. (27), the safety factor *Fs* is assigned the value of 1.25, considering that three computational grids have been utilized in the grid sensitivity analysis. Additionally, the linear grid refinement factor *r* is determined to be the square root of 2, as the coefficient of the intermediate medium grid is also $\sqrt{\mathbf{2}}$. The value of *p* is set to 2 as a result of employing second-order differential schemes in all CFD simulations; u_i means wind speed measured in the two grids; U_{ref} denotes the reference wind speed which equals 0.6 m/s.

Fig. A1 compares the wind speed profile at the location (x = 10 m). Furthermore, the height-averaged GCI averaged for the medium-fine grid is 8% at x = 10 m, and for the medium-coarse grids, the value is 0.92%. These data represent the vertical profiles of velocity as time-averaged velocity distributions. The grid converged to a satisfactory level of independence with a criterion of GCI <0.5%. Therefore, the results indicate minimal disparity in velocity between the medium and fine grids, implying that the resolution of the medium grid is sufficient to capture the key features of the simulation cases.

3.2. Model validation

3.2.1. Validation of mathematical model

In Fig.A2, a three-dimensional water tank experiment can be used here for verification [41]. The model and boundary conditions are set in line with the experiments. The slope angle is 20° and the slope is 0.175 m long. A rectangular electric heater with a length of 0.300 m is utilized to simulate the UHI, and it is connected to an appropriate power supply. Because of the heater's geometry, in the absence of other circulation, the flow linked with the simulated UHI is anticipated to be almost two-dimensional plane [41]. The boundary conditions, computational approaches and grid division principles (y+, grid stretching ratio - r) used are the same as in Section 2.2.

Fig.A3(a)(b) presents a comparison between the CFD simulation results and the corresponding experimental data for velocity profiles at locations A and B. A large difference in the velocities of the slope near the ground can be found. The velocity increased with time, being faster during the earlier periods (from 0 to 120 s after the experiment started), and gradually increasing in velocity over the remaining duration. Although there are some differences between the simulation results and the experimental results, the overall trend is consistent.

The accuracy of these three turbulent models was quantitatively assessed using a set of validation metrics (Table 2): Fractional Bias (*FB*), Fractional Accuracy Factor 2 (*FAC2*), and Pearson Correlation Coefficient (*R*). These metrics were calculated utilizing data from both CFD simulations and water tank experiment. Alongside benchmark values, the study also incorporated the following acceptance criteria: $FB < 1.5$, $FAC2 > 0.5$, and $R > 0.8$ [42]. Table 2 indicates that the model meets the requirements for predicting the flow field.
<Table.2>

In spite of there are some minor discrepancies between the results obtained from the two-dimensional and three-dimensional simulations, the two-dimensional simulations are still able to capture the primary characteristics of the heat island flows over hillslopes. Under specific conditions, the 2D simulation outcomes can be regarded as being in overall concurrence with the 3D simulation [8].

3.2.2. Validation of pollutant dispersion model

In order to further validate the accuracy of pollutant dispersion simulations, a comparison was made with another study from the literature that investigated buoyancy-driven urban ventilation [43]. Cases with a building aspect ratio of 1 were chosen for comparison, and the values of air changes per hour (ACH) at the top of street canyons were compared. It was observed that the simulated values closely approximated the literature values, with a ratio near 1:1 (Fig. A4). This indicated that the computational model exhibited a high level of accuracy.

4. Results and discussion

This study aims to assess the influence of atmospheric conditions, urban location, and urban/slope underlay materials on the coupled flow characteristics of slope winds and urban heat islands. The diurnal variations in slope winds classify them into katabatic and anabatic wind. An in-depth analysis of the factors influencing urban ventilation is conducted for each type of slope wind, followed by an exploration of their impact on the intensity of urban heat island.

4.1. Quantitative evaluation parameters for urban canopy ventilation

In order to provide a quantitative assessment of pollutant concentration in urban canyons, the air change rate per hour (ACH), local mean age of air (τ_p) and purging flow rate (PFR) are employed as evaluation metrics [44].

4.1.1. Air change rate per hour (ACH_{mean} and ACH_{turb})

$$ACH_{\text{mean}} = \frac{3600 Q_{\text{mean}}}{vol} \quad Q_{\text{mean}} = \int \vec{V} \cdot \vec{n} dA \tag{28}$$

$$ACH_{\text{turb}} = \frac{3600 Q_{\text{turb}}}{vol} \quad Q_{\text{turb}} = \pm \int 0.5 \sigma_u dA \tag{29}$$

In these formulas, Q_{mean} and Q_{turb} are the volume flow of the street valley ($m^3 . s^{-1}$). ACH_{mean} and ACH_{turb} are two hourly air change rates, which are determined

by the volume flow (m^3. s^{-1}) of the mean flow (Q_{mean}) and turbulence fluctuation (Q_{turb}) passing through the urban canopy boundary, respectively.

Where $\vec{V}$ represents the velocity vector, A denotes the surface area, and the normal direction of the room opening or the street roof is taken into account; σ_u represents the wave velocity within the urban canopy, and it is estimated based on the isotropic turbulence approximation ($\sigma_u = \sqrt{\overline{u'u'}} = \sqrt{\overline{w'w'}} = \sqrt{2k/2}$, and k is the turbulent kinetic energy).

4.1.2. Local mean age of air (τ_p)

Local mean age of air (LMAA) represents the time it takes for an air mass to travel from its entry into a specific watershed to its arrival at a particular point within the watershed, and can also be interpreted as the time it takes for external clean air to reach a designated location. Therefore, a longer air age indicates that clean air from the external environment takes a longer time to reach that point, implying poor pollutant removal efficiency [45].

There are various computational methods available, but in this study, the uniform release method is employed to calculate the air age within the urban boundary layer. This method assumes the presence of a uniformly distributed and stable pollutant source throughout the entire urban boundary layer.

$$LMAA = \frac{\langle \overline{c} \rangle}{Q} = \frac{\int_V^- cdxdydz}{V \times Q}(s) \tag{30}$$

This computational method is mathematically equivalent to its original definition [46].

4.1.3. Purging flow rate (PFR)

The LMAA provides a highly intuitive representation of the ventilation capacity within a building complex. However, for a comprehensive analysis of the overall ventilation capacity, a new evaluation parameter, termed Purging Flow Rate (PFR), is required [47]. The PFR represents the rate at which pollutants are transported out of the urban boundary layer. Its calculation formula is as follows:

$$PFR = \frac{S_P Vol}{\int_{vol} \overline{c} dxdydz / Vol} \tag{31}$$

Although the PFR calculation formula includes a term for pollutant concentration, it is actually an independent variable that represents the overall ventilation capacity within the urban boundary layer due to the combined effects of mean flow and turbulent fluctuations.

*4.2. Effect of different atmospheric layer*s

4.2.1. Katabatic winds

4.2.1.1. Urban air quality

The katabatic wind can be described as a low-level jet within the stratified atmosphere [48]. In this section, the diverse effects of katabatic winds on urban ventilation under various atmospheric stability conditions were quantified. The stability of the atmosphere is dependent on the ratio of the temperature lapse rate (γ) to the dry adiabatic lapse rate (g/cp), where a stable layer is present when γ is less than g/cp. In the troposphere, the standard vertical temperature lapse rate is 6.5K/km.

The diffusion process of pollutants inside the street valley is not only related to the flow structure, but also to the corresponding flow velocity. Since the ventilation process within the two-dimensional street valley is directly influenced by the vertical flow at the top of the valley, Fig. 2a gives the flow velocity in the vertical direction within the street valley in the urban center area. The velocities above the city are significantly higher than those within the canyons. This has significantly impacted the heat and pollutant emissions of the city.

<Fig.2>

<Fig.3>

Fig. 3a illustrates the distribution of LMAA and ACH in different atmospheric stability conditions within urban areas. The pronounced increase in vertical velocities above the city directly results in an enhanced ACH as atmospheric stability weakens. ACH under neutral atmospheric conditions can reach twice that of the inversion situation.

The general expectation is that an increase in ACH would accelerate pollutant emissions and consequently reduce LMAA. However, this is not the case as depicted in the figure. It can be observed that, with a decrease in atmospheric stability, LMAA within street canyons actually increases significantly. To comprehend this phenomenon, an analysis of the flow conditions linked with katabatic winds can be undertaken. From Fig. 4a, it is evident that katabatic winds create a temperature inversion layer above the urban street canyons, inhibiting the development of vertical convective motion. As the temperature lapse rate increases, the activity of valley winds intensifies, leading to a thickening of the inversion layer (Fig. 4b), further impeding the dispersion of pollutants. The flow within the street canyon transitions from a multi-vortex structure to a single-vortex dominance (at $\gamma = 6.5, 9.8$), generating small vortices in the corners of the street canyon. Although these corner vortices are relatively small in size, they contribute to local accumulation of pollutants. Therefore, with an increase in atmospheric instability, the emissions of pollutants within the urban block are actually restricted.

<Fig.4>

In comparison with existing literature, it becomes evident that the velocity contour plots in this study align closely with the trends observed in Luo et al.'s research. This

correspondence serves as indirect confirmation of the accuracy of the model employed in this study.

The Fig. 3b demonstrates PFR in different street canyons, thereby further investigating the effects of pollutant emissions in different locations. It can be observed, consistent with LMAA, that the PFR decreases with increasing atmospheric lapse rate in street canyons farther away from the slopes, specifically from Block 10 onwards. However, in areas closer to the slopes, the PFR exhibits an opposite trend, with the peak value increasing with an increase in γ. As indicated in the Fig. 3b, katabatic winds create a cold air pooling region on the windward side of the 0th canyon as a result of gravity. At the top of this region, cold air flows upward along the windward face of the buildings, forming a curved cold zone at the top. An increase in γ (and instability) leads to the expansion of this region. Within this region, the street canyon can effectively exchange air with the atmosphere above, facilitating the diffusion of pollutants. After No.10 street blocks, the level of pollutant purification within the street canyon becomes similar and shows no significant change, especially under stable atmospheric conditions.

4.2.1.2. Urban heat island intensity

In this section, the effects of katabatic winds on the intensity of the urban heat island (UHI) under different atmospheric stability conditions are examined. To calculate urban heat island intensity, two distinct control volumes are defined: the first one includes the entire urban area, which is represented by the urban canopy domain shown in Fig. 1, and the second one is located at the pedestrian level, which is 1.5 m above the ground surface.

Due to the presence of vortices in the street valley, the exchange of heat on both sides of the top of the street valley can only occur through diffusion. Fig. 3e illustrates the average temperatures of the urban canopy layer (UCL) and pedestrian layer (PL) under different atmospheric stratifications. As depicted in the figure, a stable atmosphere limits the release of urban heat. The average temperature difference in the city can be as high as 3.7K, while in the pedestrian layer, it is 2.8K. Notably, in a neutral atmospheric state, the temperature of the urban canopy layer decreases significantly, nearly 4K lower than in the case of a temperature inversion.

From this, it can be concluded that the dissipation of heat in the pedestrian layer is less influenced by an active atmosphere, while urban areas are more significantly affected. In neutral conditions, the difference between the two effects is most significant, being 2–3 times greater than in the remaining cases. This can be attributed to the large-scale vortex formed at the top of the urban canopy layer in a neutral atmosphere, which results in an increased air exchange rate in the vertical direction, helping to more effectively remove urban heat.

Meanwhile, a linear regression analysis of the average temperatures and temperature lapse rate is performed in the Fig. 6e and the third order polynomial relationship is as follows:

$$Tmean = A1 + B1 \times \gamma + C1 \times \gamma^2 + D1 \times \gamma^3 \quad (32)$$

In the instances presented in Table 3, when the third-order polynomial function with an R-squared value greater than 0.95 is used, it signifies that the fitted curves are well-suited and are capable of representing the third-order polynomial correlation between the average temperatures and temperature lapse rate.

<Table.3>

4.2.2. Anabatic winds

4.2.2.1. Urban air quality

In this section, the diverse effects of anabatic winds on urban ventilation under various atmospheric stability conditions were quantified.

Fig. 3c displays the dispersion pattern of LMAA and ACH across urban areas under varying atmospheric stability conditions. It can be found that LMAA within the canopy layer decreases with a decrease in atmospheric stability, indicating that weakened atmospheric stability is advantageous for pollutant emissions in urban areas. Meanwhile, the trend of ACH follows a similar pattern. Due to the minor differences in velocity above the urban area, it can be inferred that the urban area experiences relatively uniform airflow (Fig. 5a). As atmospheric stability decreases, the ventilation rate in urban areas also increases. Moreover Fig. 4d illustrates the impact of anabatic winds on the ventilation effectiveness in different locations within the city. It can be observed that except for neutral atmospheric conditions, in all other cases, as the distance from the slopes increases, the pollutant emissions within the street canyons improve progressively. These phenomena differ from the katabatic winds. The explanation is as follows.

<Fig.5>

Compared to katabatic winds, anabatic winds exhibit a distinctive layering structure that is influenced by spatial and temporal effects. Specifically, for stable atmospheric conditions ($\gamma = -1$, 0, 3K/km), there are velocity maxima above the city (40 m) and above the boundary layer (100 m), indicating a stable laminar structure. Similar to katabatic winds, increasing the atmospheric stability (γ) leads to an increase in the mixing height of the urban boundary layer, as shown in Fig. 5b. Conversely, under active atmospheric conditions, the vertical airflow movement is more dynamic, effectively enhancing pollutant emissions and improving ventilation efficiency. Moreover, due to the active atmospheric activity, the anabatic wind under neutral stratification exhibits the fastest climbing speed in the same time period, showcasing the best ventilation performance.

4.2.2.2. Urban heat island intensity

In this section, different impacts on urban heat island (UHI) effects of anabatic winds are· focused which under different atmospheric stability. Fig. 3e shows the average temperatures of the urban canopy layer (UCL) and pedestrian layer (PL) under different atmospheric stability. It can be observed that as atmospheric stability weakens, the UHI intensity decreases (by 4K for the urban area and nearly 1K for the pedestrian layer), effectively enhancing the dissipation of urban heat.

Simultaneously, a linear regression analysis is conducted on the average temperatures of the urban canopy layer and temperature lapse rate. In this case, the polynomial function with an R^2 value more than 0.95 is also adequate to depict the association between the average temperatures of the urban canopy layer and.

Compared to the temperature associated with katabatic winds, it can be observed that under different atmospheric conditions, katabatic winds are more effective in reducing urban heat island intensity, while anabatic winds have the opposite effect. Katabatic winds bring cold air from the slopes and have higher wind speeds, thereby reducing the urban heat island effect. Conversely, anabatic winds have slower wind speeds, and their stable layering structure restricts the vertical movement of air, limiting the dissipation of urban heat.

In Section 4.2, it was observed that both katabatic wind and anabatic winds result in poor ventilation capacity for the city under the condition of an inversion layer. Additionally, the urban heat island effect is strongest under these conditions. Therefore, in the subsequent investigation of influencing factors, the atmospheric environment was consistently set to temperature inversion condition in order to explore the relationship between slope winds and the urban heat island during severe and extreme weather conditions.

Considering that the ventilation level within the street canyon varies significantly within the first ten street blocks, and that there is no significant change in pollutant purification within the street canyon after the development of slope winds beyond ten street blocks, the analysis of these results is not meaningful. Moreover, in order to save computational costs, the subsequent work will reduce the size of the urban area to ten street blocks.

4.3. Effect of relative location of slopes and cities under inversion atmospheric conditions

4.3.1. Katabatic winds

4.3.1.1. Urban air quality

In this section, the impact of katabatic winds on urban ventilation under different relative positions between the city and the slopes was quantified. The overall size of the city was set as H, and the distance between the slopes and the city was set as L. L/H was used as a measure to evaluate the relative position of the city with respect to the slopes. As shown in Table 1, a total of five cases with different distances were considered.

From Fig. 6a, it can be observed that as the distance between the city and the slopes increases, LMAA decreases gradually, by approximately 500 s. As described in section 4.2.1.1, with higher wind speeds associated with katabatic winds, the inversion layer above the city becomes more stable, leading to a weakening of vertical convective motion and making it challenging for pollutants to be expelled. As the distance between the city and the slopes increases, the katabatic winds speed above the city gradually decreases, and the horizontal airflow transitions from being steady

to fluctuating. This change enhances vertical convective motion, thereby accelerating the removal of pollutants within the street canyons.

<Fig.6>

ACH, on the other hand, exhibits a different behavior. Since ACH calculation includes the 0th canyon, the flow conditions in front of the city also affect the overall ventilation rate. From the Fig. 4c, it can be observed that as the distance increases, the impact of katabatic winds on the city diminishes, resulting in a larger stagnant flow zone ahead of the city. Simultaneously, the decrease in flow velocity above the street canyon also leads to a reduction in the ventilation rate. Therefore, as shown in Fig. 6a, it can be noticed that ACH reaches its maximum at position L/H = 0.1 and gradually decreases thereafter.

The overall trend of PFR in Fig. 6b aligns with that of LMAA. However, it is noteworthy that as the distance from the slopes increases, the stagnant flow area above the city diminishes, resulting in a weakened ventilation capacity within the street canyons. As the distance increases, the promoting effect of katabatic winds on pollutant emissions in the front part of the city is weakened, and the inhibiting effect in the rear part of the city is also weakened. Consequently, the rate of PFR change in street canyons No.1-3 becomes slower.

4.3.1.2. Urban heat island intensity

Fig. 6e illustrates the average temperature variations in the urban area and pedestrian layer at different positions within the city under katabatic winds conditions. Overall, it can be observed that as the distance increases, both the urban area and pedestrian layer experience an upward trend in temperature. The most significant changes occur in the range of L/H = 0.1–1, followed by a gradual decrease in the rate of change. Particularly, when L/H = 1 and 2, the temperature in the urban area remains nearly constant. This is attributed to the decrease in wind speed with increasing distance, which reduces the ability to remove urban heat. Simultaneously, the impact of cold air from the slopes diminishes, and the urban heat island circulation dominates during these conditions.

Concurrently, an analysis using linear regression is performed to investigate the relationship between average temperatures and L/H, revealing a polynomial relationship of third order:

$$T_{\text{mean}} = A2 + B2 \times \left(\frac{L}{H}\right) + C2 \times \left(\frac{L}{H}\right)^2 + D2 \times \left(\frac{L}{H}\right)^3 \tag{33}$$

The correlation coefficients are presented in Table 4. In this instance, the polynomial function, which exhibits an R^2 value exceeding 0.95, adequately captures the relationship between the average temperatures of the urban canopy layer and *L/H*.

<Table.4>

4.3.2. Anabatic winds

4.3.2.1. Urban air quality

Anabatic winds at various city-slope distances significantly influence urban ventilation. LMAA decreases with greater distance, indicating improved pollutant emission efficiency. In the range of L/H = 0.05–0.1, a drop of around 300s occurs, followed by minor variations. Closer distances result in faster anabatic winds and a single vortex in street canyons. Distant locations exhibit consistent flow patterns. Fig. 4e shows larger vortices ahead of the city, enhancing ventilation efficiency.

Fig. 6d quantifies the pollutant removal capacity in different regions of the city. The overall trend remains consistent, with increasing PFR values from Street Canyons 1 to 9. The velocity cloud maps also indicate that the anabatic winds generally maintain higher speeds above Street Canyons 1–5, while a bulging effect is observed above the subsequent canyons, facilitating pollutant dispersion in line with the PFR trend. As the distance increases, there is an occurrence of airflow uplift in the upper part of the city's front, intensifying the longitudinal development of airflow within the street canyon and to some extent improving the suppressed ventilation condition. Therefore, in the front part of Fig. 6d, there is a change in the relative relationship of No.1.2's PFR with increasing distance between the slopes and the city. Additionally, at L/M = 0.5, 1.0, and 2.0, except for Canyon No.1, the values are relatively similar in the other canyons. This suggests that once the city reaches a certain distance from the slope, anabatic wind's efficiency in pollutant removal reaches a marginal effect, and further distance does not lead to significant changes.

4.3.2.2. Urban heat island intensity

Consistent with the phenomenon observed under katabatic winds, the average temperature of the urban area under anabatic winds also increases with distance due to the reduction in wind speed and the urban heat island effect. The most significant temperature variations occur within the range of L/H = 0.1–0.5. In comparison to other influencing factors, the relationship between anabatic winds and pedestrian-level temperatures in the city differs noticeably with increasing distance. As cooling on the mountain slope occurs rapidly during the night, cold air is funneled into the city, thereby reducing the intensity of the urban heat island. However, from Fig. 6e, it is evident that when L/H = 1 and 2, the pedestrian-level temperatures under anabatic winds are lower than those under katabatic winds. This reflects the diminishing alleviating effect of katabatic winds on the intensity of the urban heat island with increasing distance, while anabatic winds facilitate better dissipation of heat from the pedestrian level. The third-order polynomial in Table 4 also exhibits a high value of R^2.

4.4. Effect of slope/city underlayment material under inversion atmospheric conditions

The characteristics of the underlying surface materials play a crucial role in surface control within urban environments. In this section, modifications were made to the underlying surface materials of both the slope and the city. Soil, moist soil, and asphalt commonly found in natural and artificial environments were selected for

simulation purposes. The material thickness and thermal properties are provided in Table 5 [[49], [50], [51], [52]].

<Table.5>

4.4.1. Katabatic winds
4.4.1.1. Urban air quality

Fig. 7a illustrates the urban ventilation conditions when modifying the underlying surface materials of the slope. It can be observed that all three materials contribute to improved urban ventilation, with the best ventilation conditions achieved when the underlying surface of the slope is made of asphalt. This observation is further supported by the cloud patterns depicted in the figure. Due to the high heat absorption capacity of soil and moist soil, an increased thermal pressure difference between the soil and the city is observed, resulting in higher wind speeds in the katabatic winds. However, the high thermal capacity of soil and saturated soil also leads to a delayed flow response. Within the same time frame, the flow within the city is insufficient, and the street canyons exhibit multiple vortex structures. In contrast, when the underlying surface of the slope is made of asphalt, the speed of the katabatic winds within the city decreases, promoting sufficient flow within the street canyons. The airflow exchange between the street canyons and the airflow above them increases significantly, facilitating the removal of pollutants. The changes in the PFR plot demonstrate that when the underlying surface of the slope is made of concrete, the pollutant removal between street canyons in the city is more uniform, while the distribution patterns of the other three materials are generally similar. The higher thermal conductivity and heat capacity of saturated soil compared to soil contribute positively to the urban ventilation effect.

<Fig.7>

Fig. 7c illustrates the urban ventilation conditions when modifying the underlying surface materials within the city. The overall trend is consistent with the observations on the slope, and it can be observed that the overall ventilation conditions are still optimal when the underlying surface material in the city is asphalt. This is further supported by the Fig. 4d, which indicate that the flow within the street canyons is more sufficient when the underlying surface material in the city is asphalt. The asphalt material increases the environmental temperature within the city, resulting in a larger temperature difference between the city and the slope, thereby enhancing the driving force for thermal pressure.

Compared to slopes, when the underlying surface materials in the city are soil and moist soil, they have a counterproductive effect on urban ventilation. Due to the lower thermal pressure, the katabatic wind slows down, resulting in reduced ventilation efficiency within the city. However, due to the presence of convection within the underlying surface and street canyons, the emission of pollutants within the street canyons is still improved. Fig. 7d also supports this observation.

4.4.1.2. Urban heat island intensity

Fig. 9 illustrates the changes in average temperatures within the city and pedestrian layer after modifying the underlying surface materials on the slope and within the city. It is observed that when the underlying surface material in the city is asphalt, the urban heat island effect is most pronounced. Conversely, when the underlying surface on the slope consists of soil or moist soil, there is a decrease in the city's average temperature. This finding highlights the cooling effect of green slopes on the urban heat island, aligning with existing remote sensing findings [53]. Furthermore, when soil and moist soil are present within the city, their cooling effect on the urban heat island becomes even more apparent. The thermal capacity of the underlying surface itself plays a significant role in altering the temperature within the city. Due to the non-linear relationship among the variables, no fitting analysis was performed on the data in this section.

4.4.2. Anabatic winds

4.4.2.1. Urban air quality

Consistent with the katabatic wind, when the underlying surface of slopes or cities is asphalt, the overall ventilation effect of the city can reach its optimum. The flow within the urban street canyons continues to be dominated by a single-vortex structure. However, a difference arises when the underlying surface materials are soil or moist soil. In such cases, the flow within the street blocks exhibits a counter-rotating double-vortex structure, resulting in a weakened ventilation capacity. Nevertheless, when soil or moist soil serves as the underlying surface within the city, compared to not changing the underlying surface material, the anabatic wind improves the ventilation conditions of the city. The wind speed of the anabatic wind is relatively higher, leading to an increase in ventilation efficiency and a reduction in LMAA (see Fig. 8c). This improvement can be attributed to the increased thermal pressure difference compared to slopes.

<Fig.8>

When the underlying surface material is present within the city, it still enhances the convective effect within the street canyons and provides the ability to remove pollutants from the city. However, it is noteworthy that from the PFR graph, it can be observed that when the city's underlying surface is cement, the ventilation capacity of street canyons 8 and 9 is weakened. It is lower than the case of moist soil.

4.4.2.2. Urban heat island intensity

The impact of different materials on urban heat island intensity under anabatic wind follows a similar trend to that under katabatic wind (Fig. 9). When the underlying surface in the city is moist soil, it has the strongest ability to reduce both urban and pedestrian-level temperatures. However, a notable difference is observed when the city's underlying surface is asphalt. In this case, the urban temperature increases significantly. This is because the material's lower thermal capacity leads to a rapid rise in urban temperature, while reducing the thermal pressure difference with the slope. As a result, the anabatic wind becomes weaker, leading to significant accumulation of heat within the city.

<Fig.9>

5. Limitations and future work

The coupling of mountain-valley winds and urban heat island circulation was investigated in this study, encompassing considerations of atmospheric conditions, city location, and properties of underlying surface materials. The main focus was on analyzing variations in urban ventilation and changes in urban heat island intensity under the influence of these factors. However, there are still some limitations in this study. The use of a 2D urban model introduces simplifications that limit the exploration of three-dimensional intricacies within the urban environment. While it captures primary characteristics, it might not fully account for the complexities of vertical interactions and flow variations that occur in reality. For instance, it may not accurately represent vertical mixing and flow behaviors above building canopies. Additionally, this study did not consider the presence of background winds, whereas in reality, background winds often exist. Incorporating background winds adds realism, enabling the examination of the interplay between slope winds and prevailing atmospheric conditions. This offers insights into how different wind regimes contribute to or alleviate heat island effects, enhancing our understanding of the coupling mechanism. Investigating the coupling or antagonistic effects between background winds and mountain-valley winds would be an interesting avenue for further research. Overcoming the constraints of the 2D model by introducing three-dimensional aspects and background winds provides a comprehensive understanding of the coupling mechanism between slope winds and urban heat islands. This insight can unveil intricate flow patterns, convective motions, and heat transfer mechanisms important for accurate modeling and predicting heat island intensities. Nevertheless, the findings of this study can contribute to the understanding of the coupling mechanism between slope winds and urban heat islands and may provide useful references for the construction of low-carbon buildings and cities.

6. Conclusions

This study employed a multi-scale model to quantify the effects of various factors, including atmospheric conditions, relative positions of cities and slopes, and urban/slope surface materials, on the interaction between slope winds and urban heat island circulation under calm wind conditions. Ventilation rate (ACH), local air age (LMAA), and average temperature were used to evaluate the ventilation, air quality, and heat island intensity, respectively.

The findings of the study demonstrate that katabatic winds have distinct unidirectional effects on promoting or inhibiting pollutant emissions in different regions of the city, and these effects are exacerbated by changes in atmospheric conditions. A higher temperature lapse rate leads to the formation of larger vortex regions above the city's near-slope area, facilitating interactions with near-slope vortices and significantly enhancing pollutant removal in this region. Conversely, in the distant region, an increased temperature lapse rate results in a thicker inversion layer, reducing vertical interactions and inhibiting pollutant dispersion. In contrast, the anabatic wind exhibits an opposite trend, with better ventilation effectiveness observed in more distant locations. Under temperature inversion conditions, factors such as the distance

between slopes and the city, as well as surface materials, also contribute to these effects to varying degrees.

For the overall urban area, Table 5 summarizes the impacts of these factors on urban heat island and urban pollution island. In the table, the first row indicates an increase in the index. If followed by an upward arrow (↑), it indicates an enhancement of the effect. The influence of urban scale and slope/city surface materials on air quality does not exhibit a singular trend but rather an optimal solution. The values in Table 6 represent the range of impact for each influencing factor. The following conclusions were drawn from the research:

(1) For the katabatic wind

<Table.6>

In terms of heat island intensity, the primary importance of influencing factors is as follows: 1) Atmospheric conditions >2) Urban location >3) Urban/slope surface materials, ranging from 4.9K–2K. Increasing atmospheric temperature lapse rate and the proportion of natural materials in urban surface contribute to mitigating the urban heat island effect. Increasing the distance between the city and the slope exacerbates the urban heat island effect.

Regarding ventilation efficiency, the main importance of influencing factors is: 1) Atmospheric conditions >2) Urban location >3) Urban/slope surface materials. Active atmospheric conditions positively impact ventilation efficiency in urban street canyons, improving about 42 h^{-1}.

For alleviating pollution islands, the importance of influencing factors can be listed as follows: 1) Urban location >2) Atmospheric conditions >3) Urban/slope surface materials. Active atmospheric conditions exacerbate the formation of the inversion layer, thereby intensifying the formation of pollution islands. Increasing the distance between the city and the slope helps to better disperse pollutants in urban street canyons, and the local air age in street valleys can be reduced by 440s.

(2) For the anabatic wind

For the intensity of urban heat island, the primary importance of influencing factors is as follows: 1) Atmospheric environment >2) Urban location >3) Urban/slope underlying material. Increasing the rate of atmospheric temperature decrease and the proportion of natural materials in urban/slope underlying can alleviate the urban heat island effect, 4.5 and 3.3K lower respectively. Increasing the distance between the city and the slope will intensify the urban heat island effect about 4.04K and 1.2K separately.

For ventilation efficiency, the primary importance of influencing factors is as follows: 1) Atmospheric environment >2) Urban location >3) Urban/slope underlying material. Active atmospheric conditions and increasing the distance between the city and the slope have a positive impact on ventilation efficiency in urban street canyons, while the other factor do not exhibit a linear relationship. When it comes to urban/slope underlying material, using artificial materials yields the best ventilation effect.

For alleviating the pollution island, the importance of influencing factors can be listed as follows: 1) Urban location >2) Urban/slope underlying material >3) Atmospheric environment. Active vertical atmospheric movements and increasing the distance between the city and the slope will accelerate the dispersion of pollution in the urban area.

This study further revealed the interactions among slopes, cities, and the atmosphere. These findings aim to explore the air quality and UHI intensity of urban streets under different weather conditions, as well as the influence of various factors on the urban environment during extreme weather events. They provide theoretical references for the design of urbans in valley cities.

CRediT authorship contribution statement

Jin Shang: Writing – original draft, Validation, Methodology, Formal analysis, Data curation. **Huai-Yu Zhong:** Methodology, Funding acquisition, Conceptualization. **Hong-Liang Zhang:** Investigation, Data curation. **Bin Li:** Visualization, Validation. **Xiao-Xue Wang:** Conceptualization. **Fu-Yun Zhao:** Funding acquisition, Conceptualization. **Yuguo Li:** Conceptualization.

Declaration of competing interest

The authors declare that they have no known competing financial interests or personal relationships that could have appeared to influence the work reported in this paper.

Acknowledgements

This research was financially supported by the Hubei Provincial Natural Science Foundation (Meteorology) Innovation Development Joint Fund Key Project (Grant No. 2022CFD016), National Key Research and Development Program of the Ministry of Science and Technology of China (Grant No. 2022YFC3801601-02), Foreign Aid Project for High-Level Cooperation and Exchange Activities of the Ministry of Science and Technology (Grant No. 202213), Natural Science Foundation of the Anhui Higher Education Institutions of China (2022AH050307), Opening Fund of State Key Laboratory of Green Building in Western China (LSKF202312), Natural Science Foundation of China (NSFC Grant No. 51778504; Grant No. U1867221).

Appendix A. (Figures in “Accuracy of multi-scale model simulation”)

<Fig. A1>

<Fig. A1>

<Fig. A3>

<Fig. A4>

Data availability

Data will be made available on request.

References

[1] H. Liu, W. Cui, M. Zhang, Exploring the causal relationship between urbanization and air pollution: evidence from China, Sustain. Cities Soc. 80 (2022), 103783.

[2] G. Qi, J. Che, Z. Wang, Differential effects of urbanization on air pollution: evidences from six air pollutants in mainland China, Ecol. Indicat. 146 (2023), 109924.

[3] H. Yang, G. Chen, D. Wang, J. Hang, Q. Li, Q. Wang, Influences of street aspect ratios and realistic solar heating on convective heat transfer and ventilation in full- scale 2D street canyons, Build. Environ. 204 (2021), 108125.

[4] F.T. Da Silva, N.C. Reis, J.M. Santos, E.V. Goulart, C.E. de Alvarez, Influence of urban form on air quality: the combined effect of block typology and urban planning indices on city breathability, Sci. Total Environ. 814 (2022), 152670.

[5] D. Huang, B. He, L. Wei, L. Sun, Y. Li, Z. Yan, X. Wang, Y. Chen, Q. Li, S. Feng, Impact of land cover on air pollution at different spatial scales in the vicinity of metropolitan areas, Ecol. Indicat. 132 (2021), 108313.

[6] Y. Abbassi, H. Ahmadikia, E. Baniasadi, Impact of wind speed on urban heat and pollution islands, Urban Clim. 44 (2022), 101200.

[7] Y. Abbassi, H. Ahmadikia, E. Baniasadi, Prediction of pollution dispersion under urban heat island circulation for different atmospheric stratification, Build. Environ. 168 (2020), 106374.

[8] S. Mei, Z. Luo, F. Zhao, H. Wang, Street canyon ventilation and airborne pollutant dispersion: 2-D versus 3-D CFD simulations, Sustain. Cities Soc. 50 (2019), 101700.

[9] G. Chen, L. Rong, G. Zhang, Impacts of urban geometry on outdoor ventilation within idealized building arrays under unsteady diurnal cycles in summer, Build. Environ. 206 (2021), 108344.

[10] M.E. Gonzalez-Trevizo, K.E. Martinez-Torres, J.F. Armendariz-Lopez, M. Santamouris, G. Bojorquez-Morales, A. Luna-Leon, Research trends on environmental, energy and vulnerability impacts of Urban Heat Islands: an overview, Energy Build. 246 (2021), 111051.

[11] T. Li, 1 - Introduction, Vehicle/Tire/Road Dynamics, Elsevier, 2023, pp. 1–14.

[12] T. Jin, Y. Liu, J. Wei, D. Zhang, X. Wang, G. Lei, T. Wang, Y. Lan, H. Chen, Numerical investigation on the dispersion of hydrogen vapor cloud with atmospheric inversion layer, Int. J. Hydrogen Energy 44 (41) (2019) 23513–23521.

[13] C. Cintolesi, D. Di Santo, F. Barbano, S. Di Sabatino, Anabatic flow along a uniformly heated slope studied through large-eddy simulation, Atmosphere-Basel 12 (7) (2021) 850.

[14] E.T. Crosman, J.D. Horel, Large-eddy simulations of a salt lake valley cold-air pool, Atmos. Res. 193 (2017) 10–25.

[15] Y. Yang, C. Ni, M. Jiang, Q. Chen, Effects of aerosols on the atmospheric boundary layer temperature inversion over the Sichuan Basin, China, Atmos. Environ. 262 (2021), 118647.

[16] L. Zhang, X. Guo, T. Zhao, S. Gong, X. Xu, Y. Li, L. Luo, K. Gui, H. Wang, Y. Zheng, X. Yin, A modelling study of the terrain effects on haze pollution in the Sichuan Basin, Atmos. Environ. 196 (2019) 77–85.

[17] Y. Jing, H. Zhong, W. Wang, Y. He, F. Zhao, Y. Li, Quantitative city ventilation evaluation for urban canopy under heat island circulation without geostrophic winds: multi-scale CFD model and parametric investigations, Build. Environ. 196 (2021), 107793.
[18] J. Hang, M. Sandberg, Y. Li, Effect of urban morphology on wind condition in idealized city models, Atmos. Environ. 43 (4) (2009) 869–878.
[19] J. Hang, Y. Li, M. Sandberg, R. Buccolieri, S. Di Sabatino, The influence of building height variability on pollutant dispersion and pedestrian ventilation in idealized high-rise urban areas, Build. Environ. 56 (2012) 346–360.
[20] Y. Kim, H. Yeo, Y. Kim, Estimating urban spatial temperatures considering anthropogenic heat release factors focusing on the mobility characteristics, Sustain. Cities Soc. 85 (2022), 104073.
[21] M. Princevac, H.J.S. Fernando, A criterion for the generation of turbulent anabatic f lows, Phys. Fluids 19 (10) (2007), 105102.
[22] Z. Luo, Y. Li, Passive urban ventilation by combined buoyancy-driven slope flow and wall flow: parametric CFD studies on idealized city models, Atmos. Environ. 45 (32) (2011) 5946–5956.
[23] Z.J. Ye, S. M, R.A. P, Effects of atmospheric thermal stability and slope steepness on the development of daytime thermally induced upslope flow, J. Atmos. Sci. 22 (44) (1977) 3341–3354.
[24] S. Wu, C. Chen, Y. Wang, Z. Yu, J. Cao, R. Zhang, H. Song, Differential effects of valley city morphology on mesoscale flow field characteristics, Build. Environ. 205 (2021), 108283.
[25] Q. Wang, Y. Wang, Y. Fan, J. Hang, Y. Li, Urban heat island circulations of an idealized circular city as affected by background wind speed, Build. Environ. 148 (2019) 433–447.
[26] Q. Wang, Y. Fan, J. Hang, Y. Li, Interacting urban heat island circulations as affected by weak background wind, Build. Environ. 160 (2019), 106224.
[27] H. Hajmohammadi, B. Heydecker, Multivariate time series modelling for urban air quality, Urban Clim. 37 (2021), 100834.
[28] D. Zhu, X. Zhou, W. Cheng, Water effects on urban heat islands in summer using WRF-UCM with gridded urban canopy parameters — a case study of Wuhan, Build. Environ. 225 (2022), 109528.
[29] R. Aghamolaei, M. Fallahpour, P.A. Mirzaei, Tempo-spatial thermal comfort analysis of urban heat island with coupling of CFD and building energy simulation, Energy Build. 251 (2021), 111317.
[30] M. Had˘ ziabdi´ c, M. Hafizovi´ c, B. Ni˘ ceno, K. Hanjali´ c, A rational hybrid RANS-LES model for CFD predictions of microclimate and environmental quality in real urban structures, Build. Environ. 217 (2022), 109042.
[31] H.J. Breedt, K.J. Craig, V.D. Jothiprakasam, Monin-Obukhov similarity theory and its application to wind flow modelling over complex terrain, J. Wind Eng. Ind. Aerod. 182 (2018) 308–321.
[32] G. Krist´of, N. R´acz, M. Balogh, Adaptation of pressure based CFD solvers for mesoscale atmospheric problems, Bound-Lay Meteorol. 131 (1) (2009) 85–103.
[33] X. Wang, Y. Li, Predicting urban heat island circulation using CFD, Build. Environ. 99 (2016) 82–97.
[34] S. Mei, C. Yuan, Three-dimensional simulation of building thermal plumes merging in calm conditions: turbulence model evaluation and turbulence structure analysis, Build. Environ. 203 (2021), 108097.

[35] L. Shindler, M. Giorgilli, M. Moroni, A. Cenedese, Investigation of local winds in a closed valley: an experimental insight using Lagrangian particle tracking, J. Wind Eng. Ind. Aerod. 114 (2013) 1–11.
[36] G.A.D.W. Issa R I, The computation of compressible and incompressible recirculating flows by a non-iterative implicit scheme, J. Comput. Phys. 1 (62) (1986) 66–82.
[37] Y. Jing, H. Zhong, W. Wang, Y. He, F. Zhao, Y. Li, Quantitative city ventilation evaluation for urban canopy under heat island circulation without geostrophic winds: multi-scale CFD model and parametric investigations, Build. Environ. 196 (2021), 107793.
[38] K.J.B. Durran D R, A compressible model for the simulation of moist mountain waves, Mon. Weather Rev. 111 (1983) 2341–2361.
[39] N. Zhang, X. Wang, Z. Peng, Large-Eddy simulation of mesoscale circulations forced by inhomogeneous urban heat island, Bound-Lay Meteorol. 151 (1) (2014) 179–194.
[40] P.J. Roache, Quantification of uncertainty in computational fluid dynamics, Annu. Rev. Fluid Mech. 1 (29) (1997) 123–160.
[41] M. Moroni, M. Giorgilli, A. Cenedese, Experimental investigation of slope flows via image analysis techniques, J. Atmos. Sol. Terr. Phys. 108 (2014) 17–33.
[42] X. Zhang, A.U. Weerasuriya, J. Wang, C.Y. Li, Z. Chen, K.T. Tse, J. Hang, Cross- ventilation of a generic building with various configurations of external and internal openings, Build. Environ. 207 (2022), 108447.
[43] S. Mei, J. Hu, D. Liu, F. Zhao, Y. Li, H. Wang, Thermal buoyancy driven canyon airflows inside the compact urban blocks saturated with very weak synoptic wind: plume merging mechanism, Build. Environ. 131 (2018) 32–43.
[44] N. Nazarian, A. Martilli, L. Norford, J. Kleissl, Impacts of realistic urban heating. Part II: air quality and city breathability, Bound-Lay Meteorol. 168 (2) (2018) 321–341.
[45] J. Hang, Y. Li, Age of air and air exchange efficiency in high-rise urban areas and its link to pollutant dilution, Atmos. Environ. 45 (31) (2011) 5572–5585.
[46] R. Buccolieri, P. Salizzoni, L. Soulhac, V. Garbero, S. Di Sabatino, The breathability of compact cities, Urban Clim. 13 (2015) 73–93.
[47] D.S. Wilks, Statistical Methods in the, 2020.
[48] F. Catalano, A. Cenedese, High-resolution numerical modeling of thermally driven slope winds in a valley with strong capping, J. Appl. Meteorol. Climatol. 49 (9) (2010) 1859–1880.
[49] R.O. Moreno, R.A. Armindo, R.L. Moreno, Development of a low-cost automated calorimeter for determining soil specific heat, Comput. Electron. Agric. 162 (2019) 348–356.
[50] J. Chen, M. Zhang, H. Wang, L. Li, Evaluation of thermal conductivity of asphalt concrete with heterogeneous microstructure, Appl. Therm. Eng. 84 (2015) 368–374.
[51] A.P. Masoumi, E. Tajalli-Ardekani, A.A. Golneshan, Investigation on performance of an asphalt solar collector: CFD analysis, experimental validation and neural network modeling, Sol. Energy 207 (2020) 703–719.
[52] N. Tang, S.P. Wu, M.Y. Chen, P. Pan, C.J. Sun, Effect mechanism of mixing on improving conductivity of asphalt solar collector, Int. J. Heat Mass Tran. 75 (2014) 650–655.

[53] S. Ghosh, A. Das, Modelling urban cooling island impact of green space and water bodies on surface urban heat island in a continuously developing urban area, Model. Earth Syst. Environ. 4 (2) (2018) 501–515.

Graphical abstract

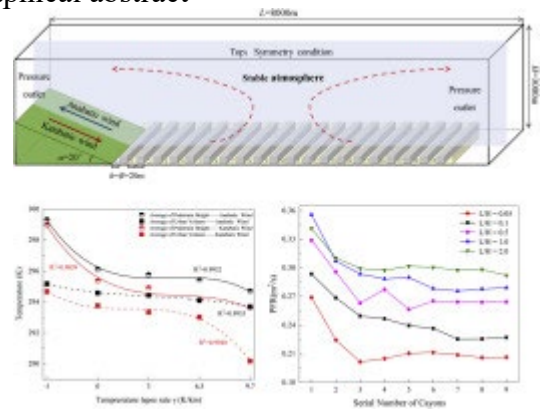

Fig. 1. Computational model for a slope with urban canyons. (a)3D sketch of the computation model: Domain is the total control volume (not to scale); (b) Grid arrangement of the simulation domain.

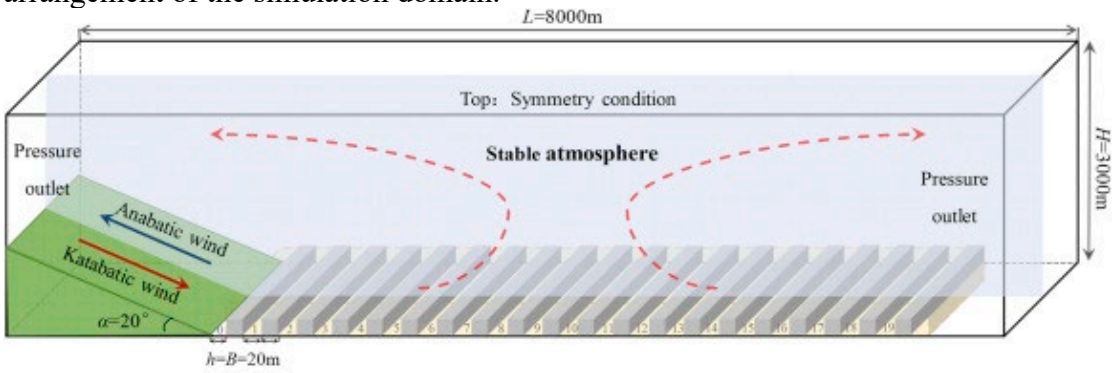

(a)

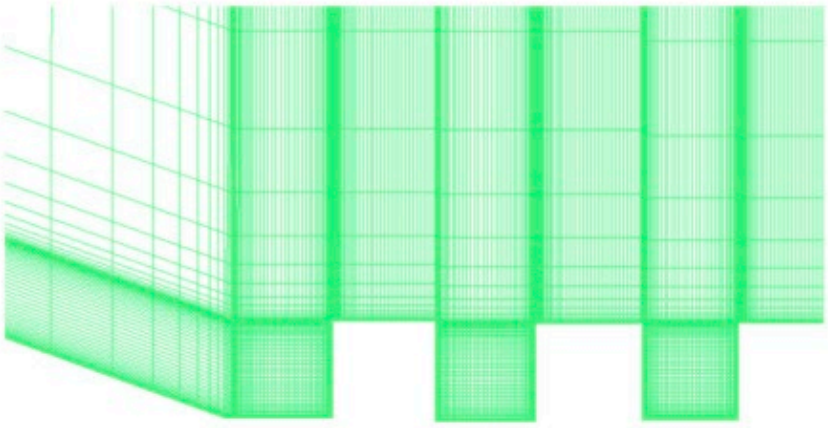

(b)

Fig. 2. Effect of katabatic winds on wind patterns under different atmospheric temperature stratification.

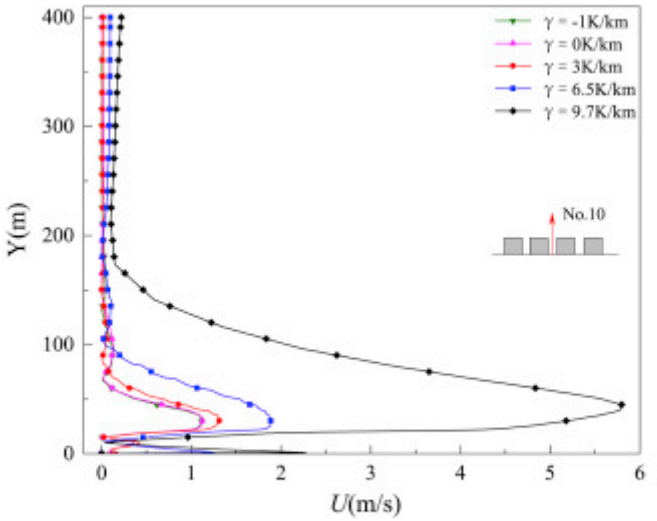

(a) Vertical wind profiles of katabatic winds in urban center areas. (No.10 canyon).

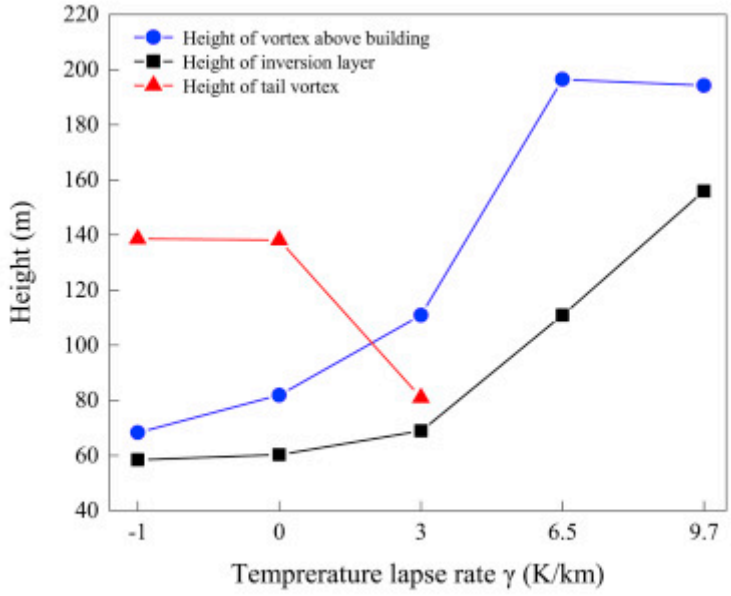

(b) Boundary layer height of katabatic winds at different locations.

Fig. 3. Indices affected by different atmospheric temperature stratification.

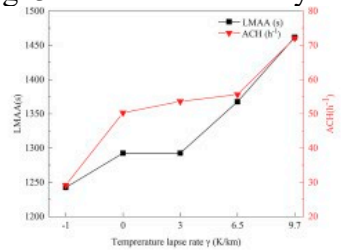

(a) Local mean age of air (LMAA) and ACH under katabatic winds affected by different atmospheric stability conditions

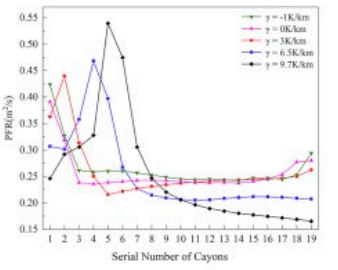

(b) Distribution of PFR in different street canyons under katabatic winds affected by different atmospheric stability conditions

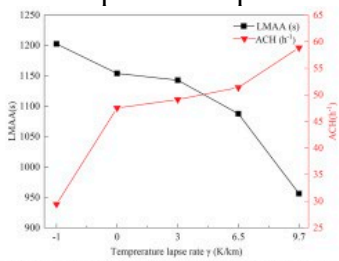

(c) Local mean age of air (LMAA) and ACH under anabatic winds affected by different atmospheric stability conditions

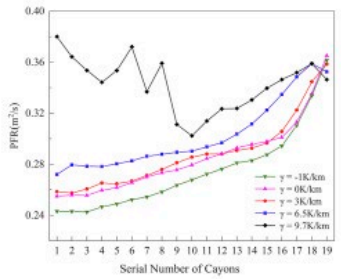

(d) Distribution of PFR in different street canyons under anabatic winds affected by different atmospheric stability conditions

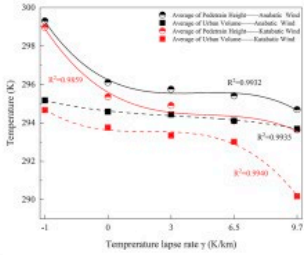

(e) Temperature distribution affected by different atmospheric stability conditions

Fig. 4. Velocity distributions and streamlines of katabatic/anabatic winds under the influence of different factors.

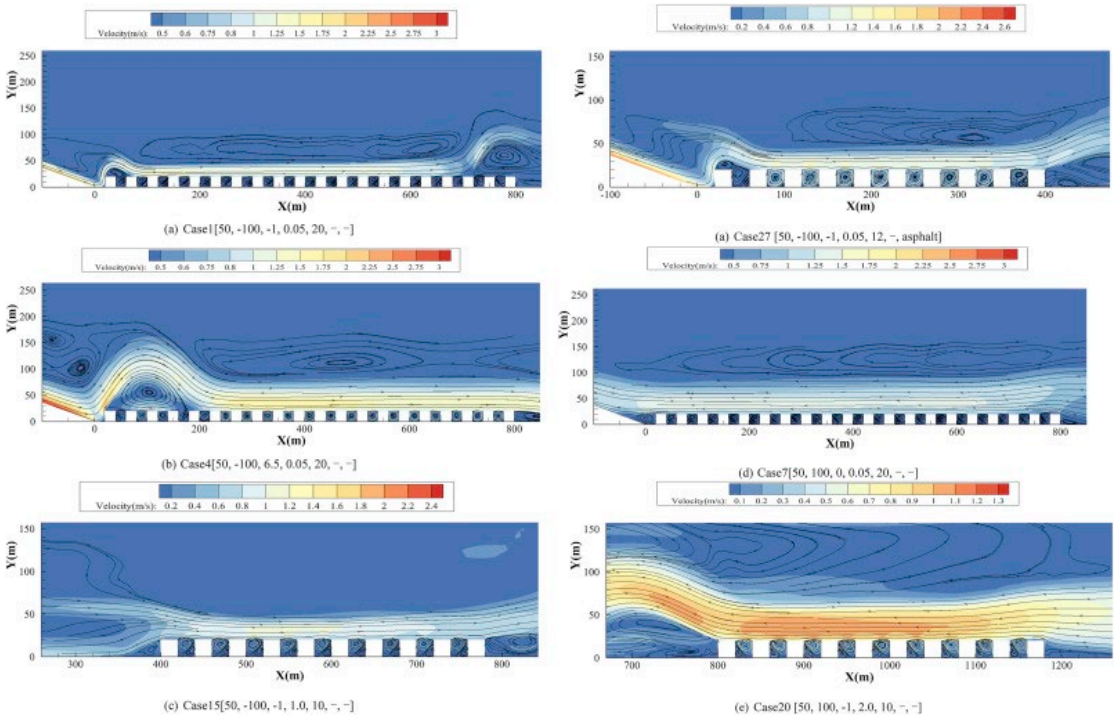

Fig. 5. Effect of anabatic winds on wind patterns under different atmospheric temperature stratification.

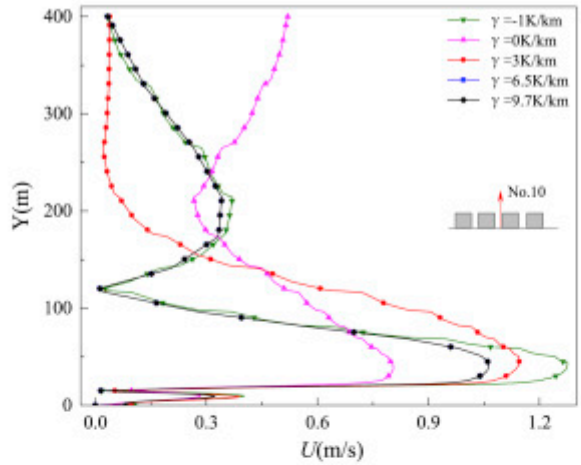

(a) Vertical wind profiles of anabatic winds in urban center areas. (No.10 canyon).

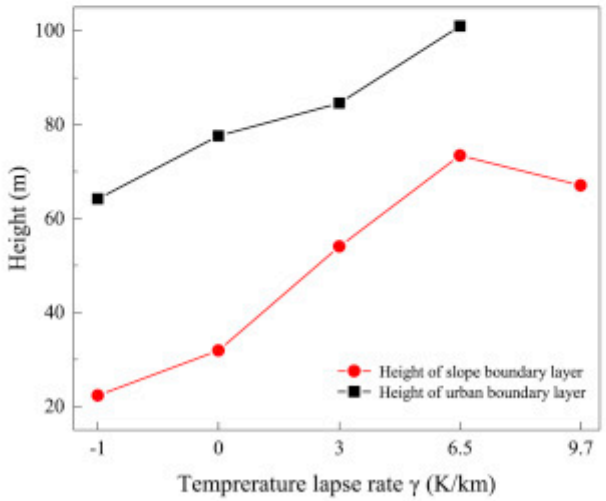

(b) Boundary layer height of anabatic winds at different locations.

Fig. 6. Indices affected by different city locations.

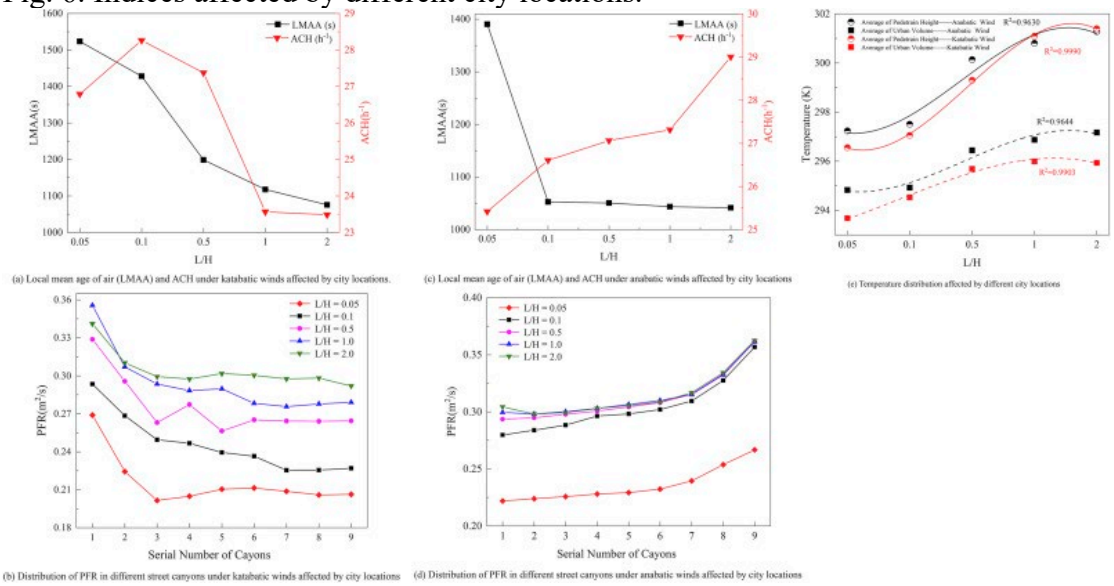

(a) Local mean age of air (LMAA) and ACH under katabatic winds affected by city locations.

(c) Local mean age of air (LMAA) and ACH under anabatic winds affected by city locations

(e) Temperature distribution affected by different city locations

(b) Distribution of PFR in different street canyons under katabatic winds affected by city locations

(d) Distribution of PFR in different street canyons under anabatic winds affected by city locations

Fig. 7. Effect of katabatic winds on urban air quality with different underlayment material.

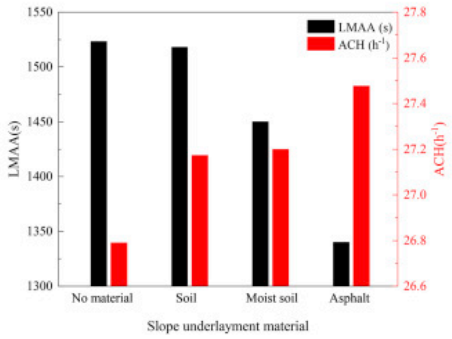

(a) Local mean age of air (LMAA) and ACH under katabatic winds affected by different slope underlayment material

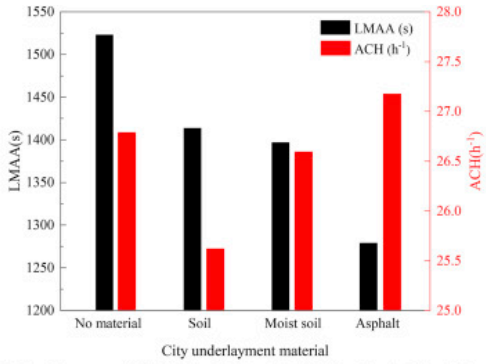

(b) Local mean age of air (LMAA) and ACH under katabatic winds affected by different city underlayment material

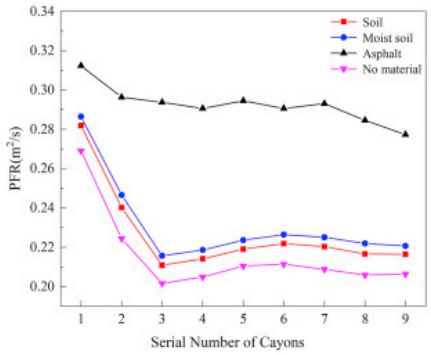

(b) Distribution of PFR in different street canyons under katabatic winds affected by different slope underlayment material

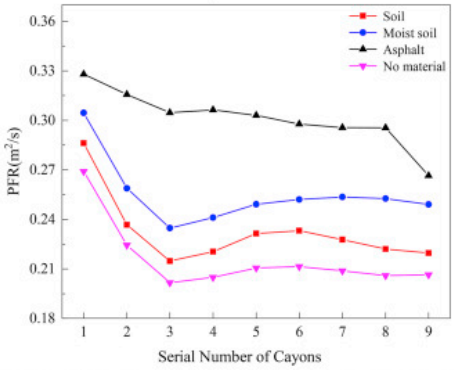

(d) Distribution of PFR in different street canyons under katabatic winds affected by different city underlayment material

Fig. 8. Effect of anabatic winds on urban air quality with different underlayment material.

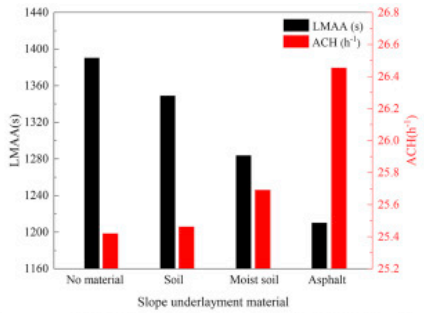

(a) Local mean age of air (LMAA) and ACH under anabatic winds affected by different slope underlayment material

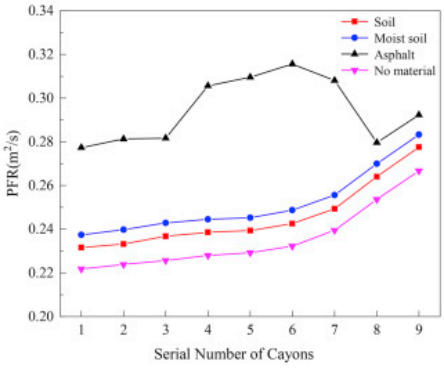

(b) Distribution of PFR in different street canyons under anabatic winds affected by different slope underlayment material

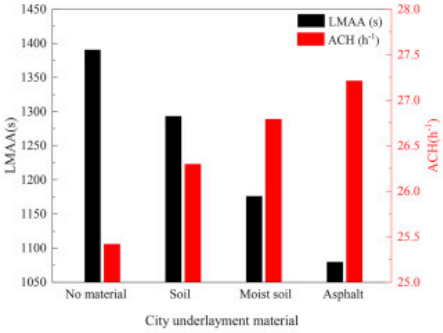

(c) Local mean age of air (LMAA) and ACH under anabatic winds affected by different city underlayment material

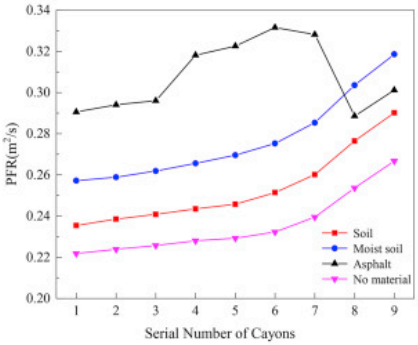

(d) Distribution of PFR in different street canyons under anabatic winds affected by different city underlayment material

Fig. 9. Influence of slope winds on urban heat island effect with different slope/city underlayment material.

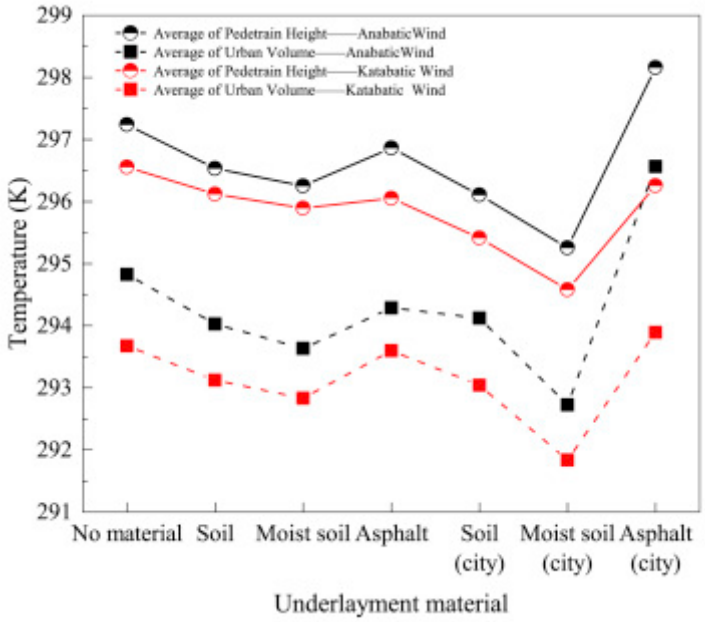

Fig. A1. Mesh independence verification of the vertical distribution of velocity at the location (x = 10 m).

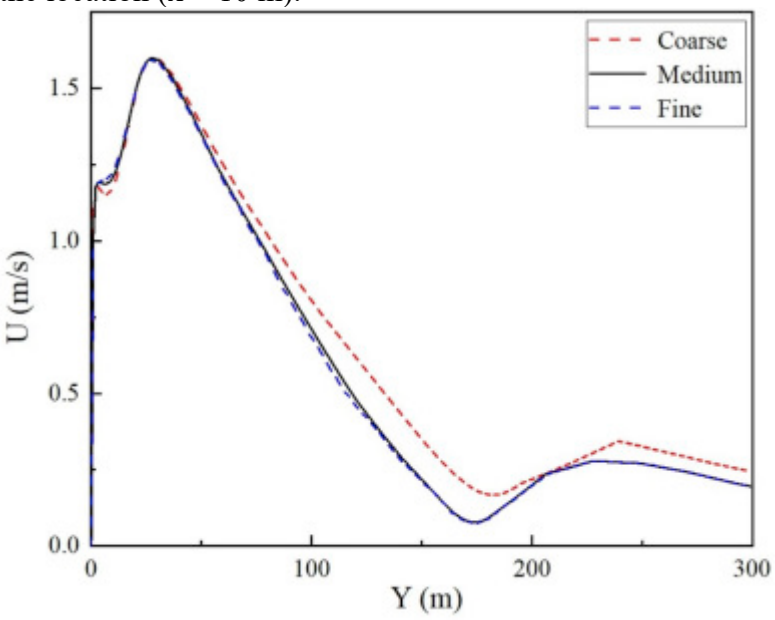

Fig. A2. Water tank experimental equipment retrieved from Ref. [41]: (a) valley model (b) reference systems and locations of velocity profiles.

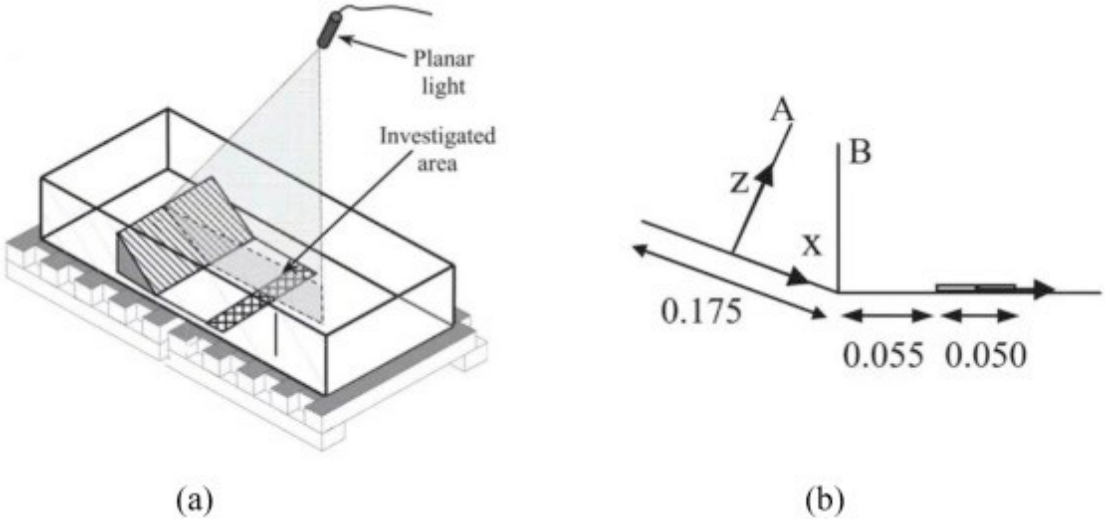

Fig. A3. Comparison of the velocity profiles between simulation and experimental data at four different moments.

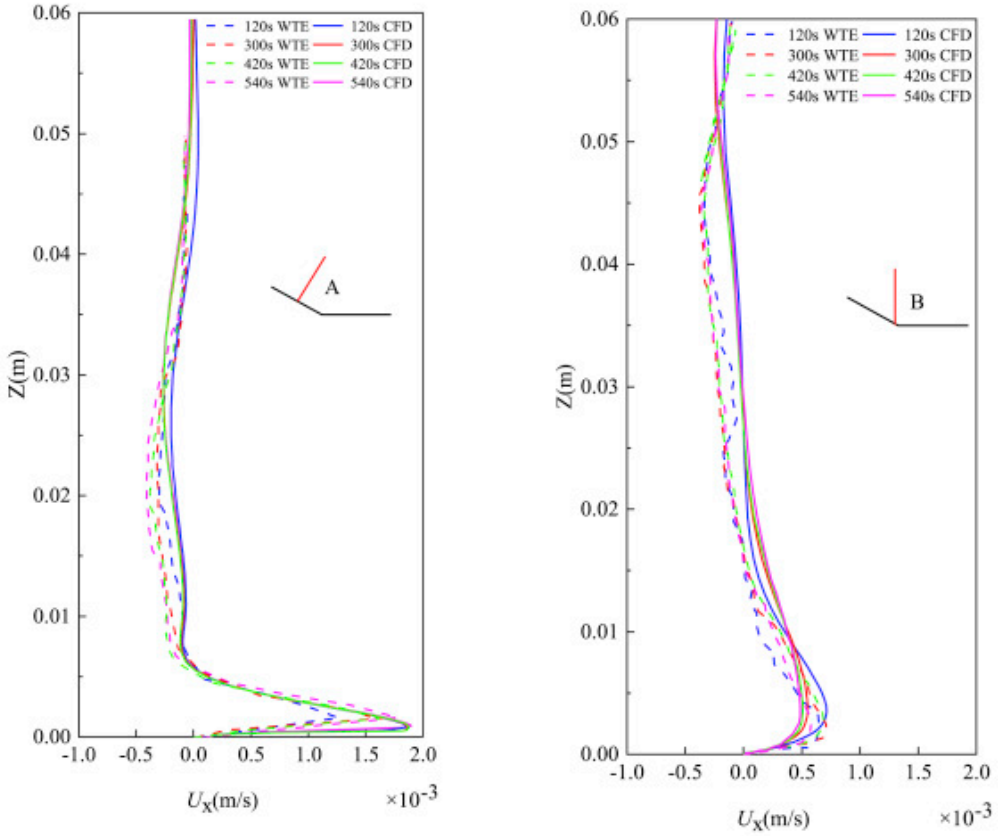

(a) Velocity profiles in location A

(b) Velocity profiles in location B

Fig. A4. Comparison between the ACH values from the literature and the simulation.

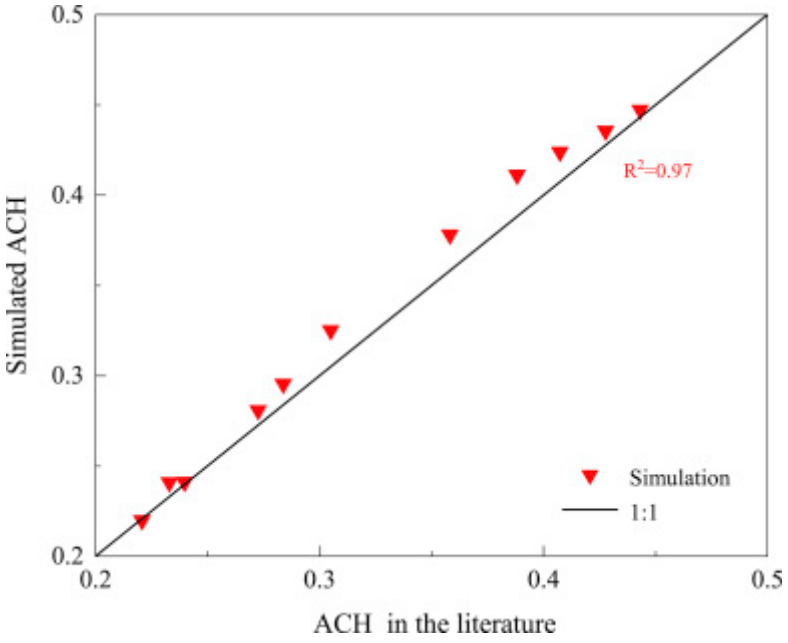

Table 1. Description of simulation cases. Each test case is defined as Case NO [urban heat flux, slope heat flux, temperature lapse rate, city location, urban scale, slope underlayment, city underlayment].

Case	Urban Heat Flux H_u ($w \cdot M^{-2}$)	Slope Heat Flux H_u ($w \cdot M^{-2}$)	Temperature Lapse Rate γ (K/km)	Atmospheric Stratification	City Location L/H	Urban Scale Number of cayons	Slope Underlayment Material	City Underlayment Material
1	50	−100	−1	Inversion	0.05	20	–	–
2	50	−100	0	Extremely Stable	0.05	20	–	–
3	50	−100	3	Stable	0.05	20	–	–
4	50	−100	6.5	Standard	0.05	20	–	–
5	50	−100	9.7	Neutral	0.05	20	–	–
6	50	100	−1	Inversion	0.05	20	–	–
7	50	100	0	Extremely Stable	0.05	20	–	–
8	50	100	3	Stable	0.05	20	–	–
9	50	100	6.5	Standard	0.05	20	–	–
10	50	100	9.7	Neutral	0.05	20	–	–
11	50	−100	−1	Inversion	0.05	10	–	–
12	50	100	−1	Inversion	0.05	10	–	–
13	50	−100	−1	Inversion	0.1	10	–	–
14	50	−100	−1	Inversion	0.5	10	–	–
15	50	−100	−1	Inversion	1.0	10	–	–
16	50	−100	−1	Inversion	2.0	10	–	–
17	50	100	−1	Inversion	0.1	10	–	–
18	50	100	−1	Inversion	0.5	10	–	–
19	50	100	−1	Inversion	1.0	10	–	–
20	50	100	−1	Inversion	2.0	10	–	–
21	50	−100	−1	Inversion	0.05	10	Asphalt	–
22	50	−100	−1	Inversion	0.05	10	Soil	–
23	50	−100	−1	Inversion	0.05	10	Moist Soil	–
24	50	100	−1	Inversion	0.05	10	Asphalt	–
25	50	100	−1	Inversion	0.05	10	Soil	–
26	50	100	−1	Inversion	0.05	10	Moist Soil	–
27	50	−100	−1	Inversion	0.05	10	–	Asphalt
28	50	−100	−1	Inversion	0.05	10	–	Soil
29	50	−100	−1	Inversion	0.05	10	–	Moist Soil
30	50	100	−1	Inversion	0.05	10	–	Asphalt
31	50	100	−1	Inversion	0.05	10	–	Soil
32	50	100	−1	Inversion	0.05	10	–	Moist Soil

Table 2. Metrics for validating wind speeds from CFD simulations.

Metric	U_x wind speed		
	FB	FAC2	R
Perfect value	0	1	1
Acceptance value	<1.5	>0.5	>0.8
Location A	0.19	0.79	0.96
Location B	0.52	0.68	0.83

Table 3. The values of the coefficients of polynomial functions (A_1, B_1, C_1 and D_1) and the value of the coefficient of determination R^2.

Configuration	A_1	B_1	C_1	D_1	R^2
T_{mean}PH_KW	298.89921	−4.90851	1.83586	−0.23542	0.9858
T_{mean}UV_KW	294.69433	−2.05111	1.23521	−0.25075	0.9940
T_{mean}PH_AW	299.2689	−4.72842	1.97	−0.26908	0.99323
T_{mean}UV_AW	295.15837	−0.77314	0.27879	−0.0445	0.9935

Table 4. The values of the coefficients of polynomial functions (A_2, B_2, C_2 and D_2) and the value of the coefficient of determination R^2.

Configuration	A_2	B_2	C_2	D_2	R^2
T_{mean}PH_KW	296.53751	−0.70993	1.56036	−0.27	0.99905
T_{mean}UV_KW	293.65297	0.88069	0.14429	−0.05583	0.99031
T_{mean}PH_AW	297.1511	−0.24558	1.1635	−0.21242	0.96299
T_{mean}UV_AW	294.77743	−0.25036	0.72671	−0.1295	0.96442

Table 5. The thermal property parameters of the slope and urban underlying surfaces.

Material	Thickness(m)	Density (kgm^{-3})	Effective thermal conductivity ($W\ m^{-1}K^{-1}$)	Effective specific heat ($Jkg^{-1}K^{-1}$)
Asphalt	2	2238	1.8	920
Soil	10	1500	1.0	1300
Moist soil	10	1950	1.85	2100

Table 6. Influence of various factors on heat island and pollution Island under katabatic wind and anabatic wind.

Katabatic wind			
	Temperature lapse rate↑	***L/H*↑**	**Slope/urban underlying surfaces material**
Heat island intensity	↓4.9K	↑4.86K	Asphalt city-max Moist soil city-min 2K
LMAA	↑224s	↓440s	No material-max Asphalt city-min 183s
ACH	↑42 h^{-1}	↑0.1-max↓ ↓4.9 h^{-1}	Asphalt slope-max Soil city-min 1.82 h^{-1}
Anabatic wind			
	Temperature lapse rate↑	***L/H*↑**	**Slope/urban underlying surfaces material**
Heat island intensity	↓4.5K	↑4.04K	Asphalt city-max Moist soil city-min 3.3K
LMAA	↓255s	↓364s	No material-max Asphalt city-min 370s
ACH	↑30.5 h^{-1}	↑3.7 h^{-1}	Asphalt city -max No material -min 1.8 h^{-1}